Diamond Precipitation Dynamics from Hydrocarbons at Icy Planet Interior Conditions

Mungo Frost,[1] R Stewart McWilliams,[2] Elena Bykova,[3] Maxim Bykov,[4] Rachel J Husband,[5] Leon M Andriambariarijaona,[6] Saiana Khandarkhaeva,[3] Bernhard Massani,[2] Karen Appel,[7] Carsten Baehtz,[8] Orianna B Ball,[2] Valerio Cerantola,[7] Stella Chariton,[9] Jinhyuk Choi,[10] Hyunchae Cynn,[11] Matthew J Duff,[2] Anand Dwivedi,[7] Eric Edmund,[12] Guillaume Fiquet,[6] Heinz Graafsma,[5] Huijeong Hwang,[13] Nicolas Jaisle,[14] Jaeyong Kim,[15] Zuzana Konôpková,[7] Torsten Laurus,[5] Yongjae Lee,[10] Hanns-Peter Liermann,[5] James D McHardy,[2] Malcolm I McMahon,[2] Guillaume Morard,[14] Motoaki Nakatsutsumi,[7] Lan Anh Nguyen,[15] Sandra Ninet,[6] Vitali B Prakapenka,[9] Clemens Prescher,[16] Ronald Redmer,[17] Stephan Stern,[5,18] Cornelius Strohm,[5] Jolanta Sztuk-Dambietz,[7] Monica Turcato,[7] Zhongyan Wu,[15] Siegfried H Glenzer,[1] and Alexander F Goncharov[12]

[1]*High Energy Density Science Division, SLAC National Accelerator Laboratory, 2575 Sand Hill Road, Menlo Park, USA*

[2]*SUPA, School of Physics and Astronomy, and Centre for Science at Extreme Conditions (CSEC), University of Edinburgh, Edinburgh, UK*

[3]*University Bayreuth, Universitätsstraße 30, Bayreuth, Germany*

[4]*Mathematisch-Naturwissenschaftliche Fakultät - Institut für Anorganische Chemie, Universität zu Köln, Greinstraße 6, Köln, Germany*

[5]*Deutsches Elektronen-Synchrotron DESY, Notkestr. 85, 22607 Hamburg, Germany*

[6]*Institut de Minéralogie, de Physique des Matériaux et de Cosmochimie (IMPMC), Sorbonne Université, CNRS UMR 7590, MNHN, 4, place Jussieu, Paris, France*

[7]*European XFEL, Holzkoppel 4, Schenefeld, Germany*

[8]*Radiation Physics / High Energy Density, Helmholtz-Zentrum Dresden-Rossendorf (HZDR), Bautzner Landstraße 400, Dresden, Germany*

[9]*Consortium for Advanced Radiation Sources, The University of Chicago, 5640 South Ellis Avenue, Chicago, Illinois, USA*

[10]*Department of Earth System Sciences, Yonsei University, 50 Yonsei-ro Seodaemun-gu, Seoul, South Korea*

[11]*Physical & Life Sciences, Lawrence Livermore National Laboratory, 7000 East Avenue, Livermore, California, USA*

[12]*Earth and Planets Laboratory, Carnegie Institution for Science, Washington, DC, USA*

[13]*School of Earth Sciences and Environmental Engineering, GIST, Gwangju, South Korea*

[14]*Univ. Grenoble Alpes, Univ. Savoie Mont Blanc, CNRS, IRD, Univ. Gustave Eiffel, ISTerre, 38000 Grenoble, France*

[15]*Department of Physics, Hanyang University, 17 Haengdang dong, Seoul, South Korea*

[16]*Institute of Earth and Environmental Sciences, Albert-Ludwigs University of Freiburg, Hermann-Herder-Str. 5, Freiburg, Germany*

[17]*Institut für Physik, Universität Rostock, Albert-Einstein-Straße 23-24, 18059 Rostock, Germany*

[18]*current affiliation: X-Spectrum GmbH, Luruper Hauptstr. 1, 22547 Hamburg, Germany*

(Dated: August 23, 2023)

Abstract

The pressure and temperature conditions at which precipitation of diamond occurs from hydrocarbon mixtures is important for modeling the interior dynamics of icy planets. However, there is substantial disagreement from laboratory experiments, with those using dynamic compression techniques finding much more extreme conditions are required than in static compression. Here we report the time-resolved observation of diamond formation from statically compressed polystyrene, $(C_8H_8)_n$, heated using the 4.5 MHz X-ray pulse trains at the European X-ray Free Electron Laser facility. Diamond formation is observed above 2500 K from 19 to 27 GPa, conditions representative of Uranus and Neptune's shallow interiors, on 30 to 40 µs timescales. This is much slower than may be observed during the ∼10 ns duration of typical dynamic compression experiments revealing reaction kinetics to be the reason for the discrepancy. Reduced pressure and temperature conditions of diamond formation has implications for icy planetary interiors, where diamond subduction lead to heating and could drive convection in the conductive ice layer which plays a role in their magnetic fields.

Hydrocarbons are found in a variety of astrophysical locations, including in icy planets and moons [1–3]. In many of these environments, such as the interiors of icy planets and during impact events, hydrocarbon-rich matter is subjected to extremes of pressure and temperature which can induce chemical reactions [4–9]. In the atmospheres of Uranus and Neptune carbon is observed at many times solar abundance and hydrocarbons have been predicted to be abundant within them [1, 2].

At high-pressure high-temperature conditions, both experimental and theoretical studies find that methane, CH_4, is converted to more complex hydrocarbons and hydrogen above a few GPa and 1200 K [4, 5, 7–11]. In addition, ethane C_2H_6, is found to form both methane and heavier hydrocarbons at similar conditions [9]. In the carbon-hydrogen system the lifetimes of molecular C-C and C-H bonds have been predicted to become short at high temperature and pressure [7], with the result that hydrocarbon molecules become very short lived and the system is better viewed as a mixture of carbon and hydrogen atoms than as persistent molecules. At the high PT conditions which occur within icy planets the carbon and hydrogen demix, and the fate of hydrocarbons deep in them is conversion to diamond and a hydrogen-rich phase [4–7].

Within icy planets, diamond formed from such reactions is denser than the surrounding ices and will sink deeper into the planet due to gravity, providing an additional source of heating which can affect their evolution and internal dynamics [4, 6, 12]. In our solar system, Neptune has higher luminosity than Uranus, pointing at an internal energy source [1, 2, 13] which could arise from the diamond formation and sedimentation. Beyond the solar system, many exoplanets have been discovered with densities matching icy planets and intermediate sizes between Earth and Neptune [14] where hydrocarbon demixing may be an important process. The conditions at which diamond precipitation occurs dictates the depth at which the diamond forms and the size and age of an exoplanet where this process will play a role in planetary dynamics.

Despite the importance of this reaction, the pressure and temperature required are subject to large disagreement in the literature, in particular between studies using dynamic or static compression techniques. Optical laser heated diamond anvil cell studies on methane find diamond formation above 10 GPa and 2000 to 3000 K [4, 5], while a study using laser-driven shocks in polystyrene found diamond formation only above 140 GPa and 4000 K [6]. The conditions determined for diamond formation in different experimental studies are

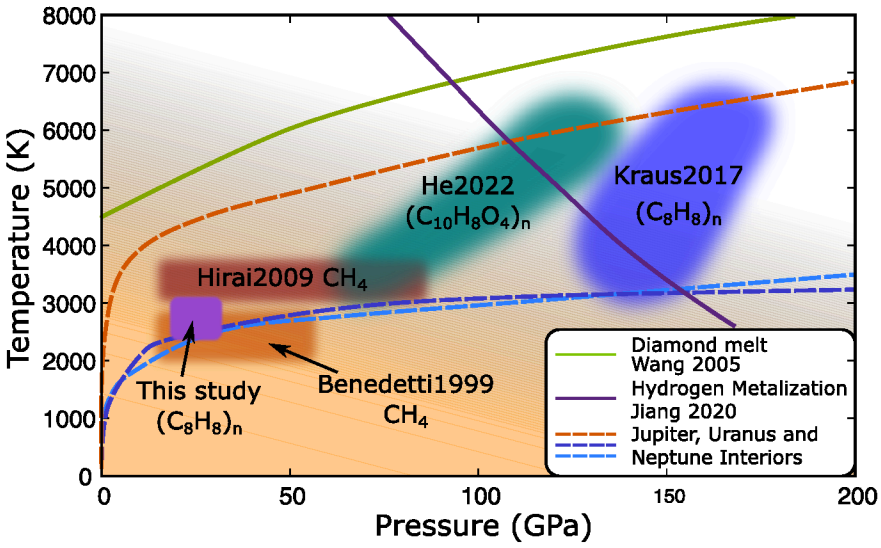

FIG. 1. State diagram of hydrocarbons at high PT showing differing conditions found to be required for diamond formation, as well as selected phase transitions (solid lines) and planetary interiors (dashed). Studies using static compression (orange area [4] and red area [5]) observe diamond formation at lower PT than shock experiments (blue area [6]), which only observe it at conditions corresponding to those where hydrogen is metallic [15]. The results presented here confirm that diamond formation can occur at conditions found in the shallow interiors of Uranus [1] and Neptune [2], including at lower estimates of the temperature conditions. The conditions for diamond formation in shocked PET, $(C_{10}H_8O_4)_n$ (teal area [16]), the diamond melt curve [17] and Jupiter's isentrope [18] are also shown.

summarized in Figure 1.

A suggested origin of this discrepancy are reactions with the metallic coupler typically used to absorb the heating laser in optical laser heated DAC studies [6]. Prior DAC studies used platinum [4, 5] which can react with hydrogen to produce platinum hydride [19] with the result that the reaction is changed from *hydrocarbon* $\longrightarrow$ *diamond + hydrogen* to *hydrocarbon + platinum* $\longrightarrow$ *diamond + platinum hydride*. The formation of metal hydrides changes the thermodynamics of the reactions and is known to promote other reactions in hydrocarbons under pressure [20]. Catalytic effects from the metallic coupler have also been suggested to play a role [10], though catalysts can only change reaction rates and not the overall thermodynamic favorability. It should be noted that not all laser heated DAC studies used a coupler. Various alkanes heated directly with a CO_2 laser exhibited diamond

formation between 10 and 20 GPa [21] and similarly heated polyethylene formed diamond at 2500 K between 10 and 30 GPa [22]. Effects arising from the presence of the diamond surface of the anvils are unlikely in studies using couplers, including this one, as the heated region is separated from the anvil surface by colder material, see Extended Data Figure 1. Prior DAC studies have investigated only samples quenched to ambient temperature after heating however, and no static compression experiment has observed diamond formation from hydrocarbons *in situ* at high temperature.

Another difference is the choice of sample. However, hydrocarbons are known to undergo reactions to form mixtures of species at PT conditions below those at which demixing to diamond and a hydrogen rich phase occur [4, 5, 7–10]. The precursor therefore determines the ratio of carbon to hydrogen. DAC studies on diamond formation from optical laser heated hydrocarbons all find the temperature required for diamond formation to be in the region of 2000 to 2500 K regardless of the initial hydrocarbon [4, 5, 21, 22]. Studies on methane and ethane find the formation of new compounds [8–10], which can be either heavier or lighter [9], in samples quenched from lower temperatures prior to diamond formation. This is consistent with the results of ref. [7], who use computational methods to simulate hydrocarbons at high PT and find that the C-C and C-H bonds become short lived and that concept of individual molecules as long-lived entities breaks down. One could therefore conjecture that, once in this state the initial material dictates the ratio of C:H based on its stoichiometry, but as the initial bonds will have broken prior to diamond formation its starting chemical structure is less important. It is worth noting that the disagreement between static and shock compression studies persists in shocked polyethylene, which exhibits no diamond formation corresponding to conditions where it is observed statically [23].

Perhaps the largest difference between the measurements of the laser heated DAC and shock compression studies is the timescale of the physical processes, which can differ by more than 10 orders of magnitude. The duration between shock compression and the probe is of order 10 ns [6, 23, 24], while laser heated hydrocarbon studies in diamond cells have taken place on timescales of seconds to minutes [4, 5, 22]. Computer molecular dynamics simulations typically study reaction processes on even shorter timescales in the sub-ns range [7, 10]. Given that diamond formation in hydrocarbons is partly diffusion-controlled, an implied rate dependence in diamond precipitation could explain differences between dynamic and static experimental observations. A dependence on timescale for diamond formation and

corresponding material properties, such as equations of state, would have major implications for diverse scenarios ranging from inertial confinement fusion [25, 26] to formation of natural impact microdiamonds [27].

Here we investigate the effect of time on diamond formation in statically compressed X-ray Free Electron Laser heated polystyrene. To avoid unwanted reactions, we use a gold coupler which forms no known hydrides or carbides. Heating occurs via a series of <50 fs high intensity X-ray pulses at 4.5 MHz [28] which also probe the state of the sample via powder X-ray diffraction [29, 30]. In this way we recover the evolution of the system in the time domain on a timescale between 220 ns and 77 µs, which is intermediate between shock and traditional laser heated DAC experiments. In doing so we characterize demixing kinetics at extreme conditions which offers insight into the process and resolves the discrepancy between prior static and dynamic compression experiments.

RESULTS

Polystyrene film was compressed in diamond anvil cells (DACs) and heated using an X-ray free electron laser (XFEL) beam absorbed by a perforated 5 µm thick gold foil coupler embedded in the sample. The experimental setup is shown in Figure 2. The temperature was measured via spectrally resolved streaked optical pyrometry (SOP) with a time window of 97.4 µs which encompasses the full 352 pulses in the XFEL pulse train [31]. SOP is a surface measurement and, as hydrocarbons darken when heated in DACs [4, 5, 8, 9, 22], it measures the temperature of the opaque envelope of the heated sample due to the large increase in emissivity during reaction [32, 33].

Thermal measurements were complemented by diffraction from the gold coupler which constrains its temperature via the thermal equation of state of gold [34]. The gold equation of state gives systematically cooler temperatures, which is expected due to differences in the temporal structure of the measurements, and is subject to 300 to 500 K uncertainty arising from the choice of equation of state, temperature gradients and thermal pressure. The upper temperature measurable by the equation of state of gold is also limited by its the melting point, about 2200 to 2500 K for the pressures in this study [35, 36]. In addition to experimental measurements, the thermal evolution of the sample was investigated using finite element analysis (FEA). The simulations indicate ±200 K thermal gradients across

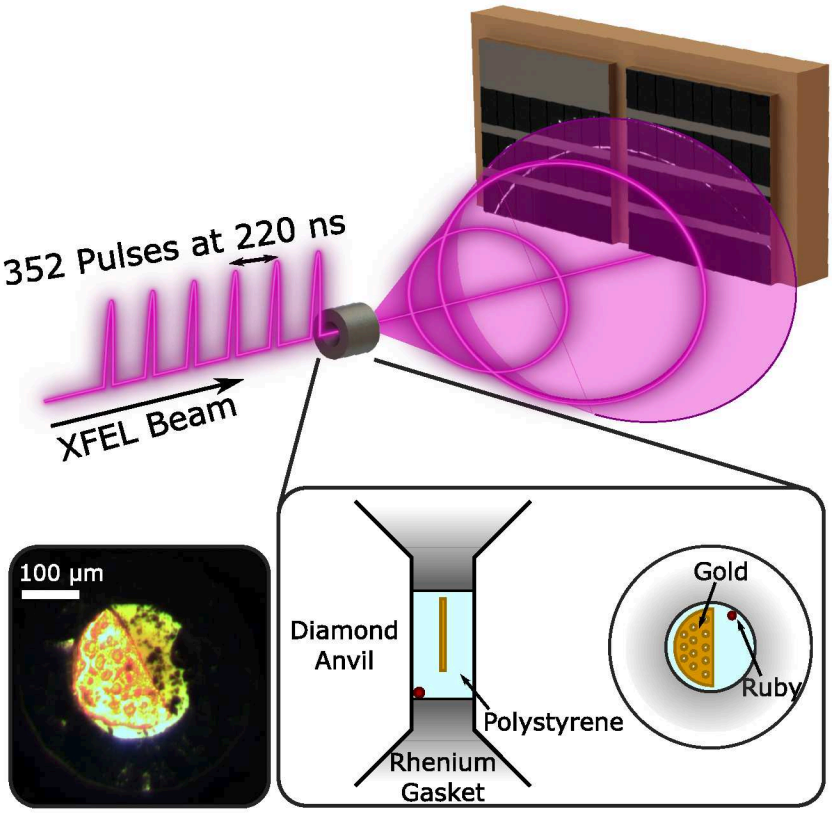

FIG. 2. Experimental setup showing the 4.5 MHz X-ray pulse train acting as pump and probe on the sample compressed in a DAC with diffracted X-rays incident on an eight-module Adaptive Gain Integrating Pixel Detector (AGIPD 500k). Enlargement shows the DAC loading configuration with the perforated gold coupler embedded in polystyrene. The inset shows a micrograph of the sample prior to the experiment.

the ∼10 µm diameter hole in the gold coupler. Time resolved data are presented in Figure 3. Additional discussions of the experiment are presented in the Methods section.

Diamond formation was determined by the emergence of the diamond {111} peak in the X-ray diffraction patterns and was observed in polystyrene which was X-ray heated above 2500 K in a pressure range of 19 to 27 GPa. Diamond formation was not observed at lower temperatures (Extended Data Figure 2) and diamond took at least 30 µs to form when this temperature was exceeded (Extended Data Figures 3 and 4). Heating for a shorter duration using a truncated pulse train (reaching 3400(300) K for 15 µs) did not result in diamond formation, confirming the requirement for sustained heating at these pressures.

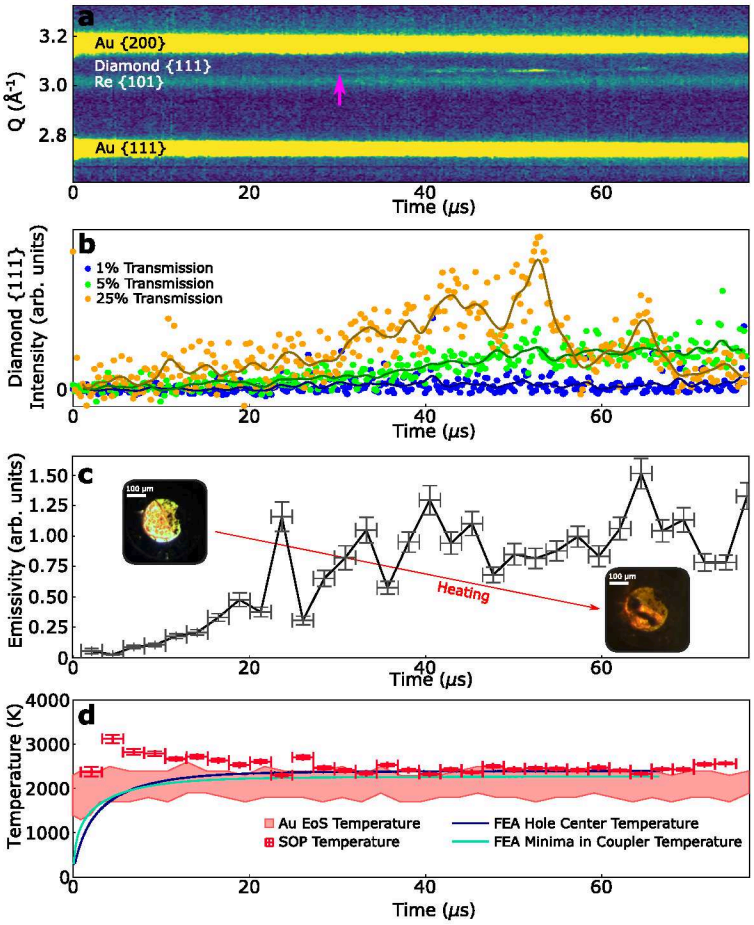

FIG. 3. Time resolved data from a run starting at 20 GPa with average pulse energy of 71 µJ. The initial XFEL pulse occurs at time 0. **a:** Integrated diffraction patterns from the AGPID detector as a function of time in region of interest, background subtracted and normalized to the beam intensity monitoring diode. Yellow shades correspond to higher intensity. The pink arrow indicates the onset of observable diamond signal. **b:** Intensity of the diamond peak as a function of time for different X-ray absorber transmissions. 25% transmission is the same run as the other panels in this figure. Lines are smoothed by a 15 pulse wide Hamming window. **c:** Emissivity increases during the run. Inset photos show the sample before and after heating.**d:** Temperature as a function of time. Bars show fitted temperatures from SOP with a 2.4 µs bin width, the error shown is the fitting error, in addition to this there is ±200 K from thermal gradients. The red region is temperature from the equation of state of the gold coupler [34], blue and teal lines are temperatures modeled using finite element analysis. Temporal error bars represent the time bin of the SOP, emissivity and temperature error bars represent one-half standard deviation confidence and are derived from the fitting uncertainty of a Planck function to the spectrographic data and statistical analysis of these data [31].

The diamond {111} peak is well suited to determine the presence of diamond as the diamond anvils are single crystals with the (100) axis aligned with the compression axis (and the XFEL beam), so that the {111} peaks of the anvils are not observed on the detector. Other diamond peaks fall outside the q range accessible in this experiment (q = 1.29 to 4.47 Å^{-1}). At early times, around 30 µs, the diamond peak is weak and requires summation over multiple integrated frames to be observed above the background. At around 40 µs larger diamond grains start to materialize as evident by distinct diffraction spots in the raw patterns, see Extended Data Figure 5. In addition to the time-resolved observation of the emergence of this peak during heating, it was also observed in the quenched sample using the highly attenuated XFEL beam. Diamond is also observed in the Raman spectrum of the recovered parts of the heated sample after removal from the DAC.

Figure 4 compares the X-ray diffraction patterns of the sample at various stages during heating. At early times no diffraction from diamond is observed, while after 40 µs there is a clear diamond {111} peak in the integrated patterns collected from individual pulses. Diamond diffraction is also observed from the sample after cooling which probed with a highly attenuated beam.

Raman spectra of the decompressed sample after removal from the diamond cell are shown in Figure 5. The first order Raman peak of diamond is clearly observed offering additional confirmation that diamond formation occurred at high PT conditions. Adjacent polystyrene which was subjected only to pressure but not heated does not exhibit this peak. Removal of the sample from the DAC is necessary to observe this peak due to the strong Raman signal from the diamond anvils.

DISCUSSION

The results offer time resolved insight into the dynamics of carbon-hydrogen demixing at extreme conditions and resolves the disagreement between prior laser heated DAC and laser driven shock experiments. We observe diamond to form from polystyrene between 19 and 27 GPa, but only after it is held above 2500 K for 30 to 40 µs. Initially summing multiple integrated frames is required to get clear diffraction from the diamond {111} peak above background, and isolated spots from individual crystallites are not observed in the raw diffraction patterns. This implies that the diamond forms a powder initially. At later

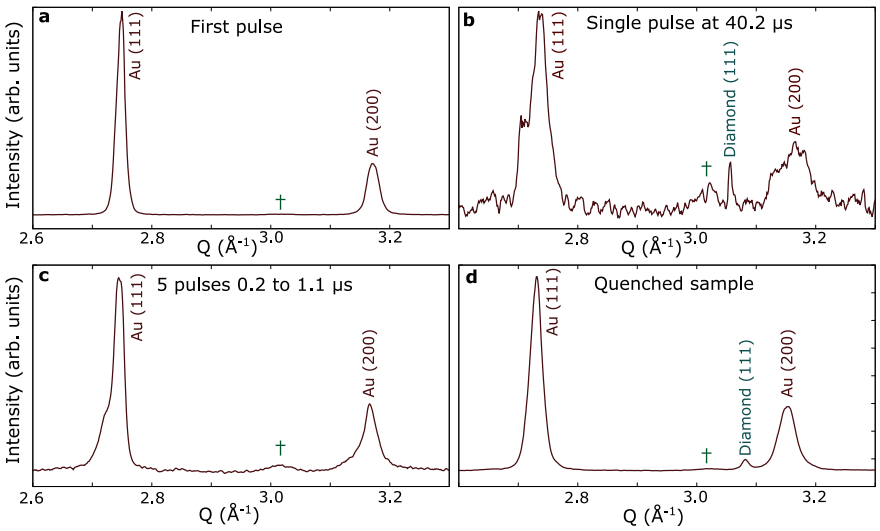

FIG. 4. Integrated X-ray diffraction patterns in the region of interest from a run starting at 19 GPa. There are no observable peaks at other q within the angular range of the detector. **a:** First pulse showing unheated and unreacted sample. **b:** Pulse 183, 40.2 µs after the first pulse, showing clear diffraction from the diamond {111} at $q = 3.056$ Å^{-1}. **c:** Sum of pulses 2 to 6 showing no diamond at early times. **d:** Diffraction from the quenched sample at 16 GPa shows a clear diamond {111} peak at $q = 3.086$ Å^{-1}. The increase in q from panel **b** to **d** is due to lattice contraction on cooling. The broad peak marked with a dagger is the rhenium {101} reflection from the DAC gasket.

times diamond diffraction is observed in single integrated frames, see Figure 4b, with visible spots of higher intensity at the diamond {111} scattering angle (see Extended Data Figure 5) implying a larger fraction of diamond and larger crystals at later times. The intensity arising from the emergence of the diamond {111} peak over three runs is shown in Figure 3b. Low pulse energies from the run with 1% absorber transmission results in negligible heating and no detectable diamond formation. Both 5% and 25% beam power resulted in heating and the emergence of diffraction signal from diamond after ∼30 µs.

In the high power runs at late times the diamond signal is observed to fluctuate. This is attributed to the increased size of the diamond crystallites at later times resulting in larger fluctuations in diffraction signal as they move and rotate within the molten region and so only intermittently fulfill the Bragg conditions. Extended Data Figure 1 shows a thermal cross-section of the sample based on FEA simulation, due to thermal gradients the region fluid hydrocarbon is larger than the hot spot where diamond formation occurs

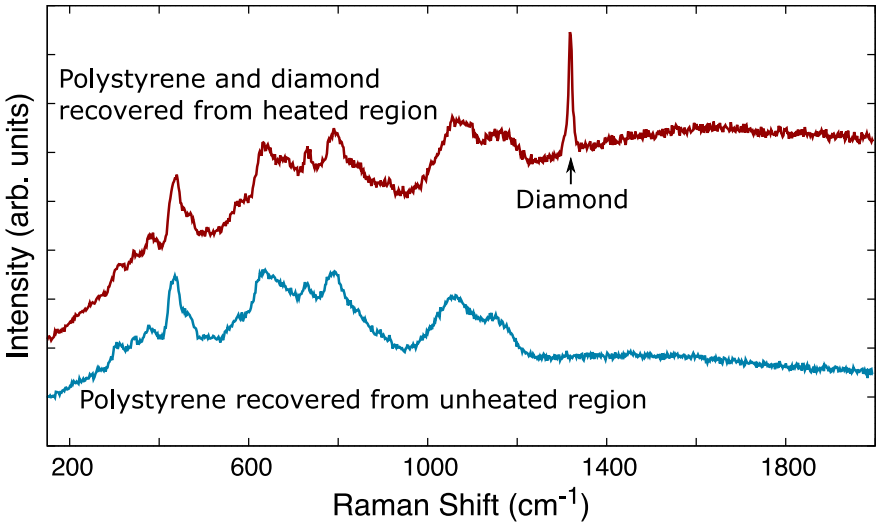

FIG. 5. Raman spectra of the sample after removal from the DAC. Previously pressurized but unheated material is in blue, while material from the heated spot is shown in red. Note the sharp diamond Raman peak present only in the material which was previously heated to 2500 K.

allowing for migration and rotation of the diamond crystallites. They can move then out of Bragg conditions or away from the the $\sim$ 10 µm coupler hole where the hot spot is centered and which is probed by the XFEL beam. Diamond is more absorbing to X-rays than the surrounding liquid hydrogen-rich phase, and the XFEL beam is (approximately) gaussian in intensity. Therefore the region of a diamond crystal closest to the beam center is most heated. This may generate a force pushing it away from beam center.

Our data enable the observation of reaction pathways unavailable previously. They agree with static experiments concerning the reaction product but in addition provide insight into the transformation in the time domain. The unique capabilities of XFEL heating to allow for the use of a gold coupler which couples poorly to IR heating lasers. There are no known compounds of gold with hydrogen or carbon so reaction with the coupler is not expected or observed, avoiding potential issues with prior laser-heated DAC studies. It has been previously proposed [6] that loss of molecular hydrogen from samples in traditional DAC experiments [5] could explain the observed difference between shock and static studies, however this argument is speculative, as is its relevance for planetary interiors where molecular hydrogen loss to the atmosphere is likely [37]. Our experiments operate on a considerably shorter timescale than traditional DAC experiments which limits the time available for hydrogen diffusion. Additionally, the barrier of cold polystyrene which encapsulates the heated

region, see Extended Data Figure 1, will further reduce hydrogen losses. This suggests an alternative reason for the discrepancy between studies using dynamic and static compression.

Instead, the disagreement appears to arise from the kinetics of the diamond formation mechanism. Laser shock compression studies typically probe timescales in the region of 10 ns, which is three orders of magnitude shorter than is required for diamond formation at lower pressures observed in this study. The formation of diamond from the high-pressure high-temperature mixture of carbon and hydrogen implies demixing. At shorter times, or lower temperatures, the sample darkens consistent with the formation of complex hydrocarbons previously observed [4, 5, 8, 9] and calculated [7, 10]. These are amorphous and not readily detected using X-ray diffraction.

The results of previous studies suggest that the timescale of diamond formation is dictated by the stability of the carbon-hydrogen fluid from which it precipitates. Dynamic compression studies observe rapid diamond formation at conditions where hydrogen is metallic [6, 15, 33, 38–40] and have inferred the presence of metallic hydrogen in the shocked material [41]. Carbon is not predicted to metallize up to much higher pressures [42] , and we speculate that the greatly decreased timescale of diamond formation in conditions where hydrogen is metallic could arise from the expulsion of non-metallic carbon from the metallic hydrogen.

Compared to prior shock experiment [6], the lower pressure and temperature required for diamond formation at longer, µs, timescales has implications for the interior dynamics of icy planets. These are known to contain methane in their atmospheres, and many models propose small molecule (H_2O, CH_4, NH_3) 'ice' mantles surrounding a rocky core [1, 2]. The formation of diamond within the mantles is proposed as a source of internal heating from phase separation of the carbon and hydrogen and subsequent gravitational heating from sedimentation of the denser diamond. However, more recent models of their interior conditions, Figure 1, suggest that the temperatures required for diamond formation in shock studies may only be reached near the cores of the local icy planets.

The conditions at which diamond formation is observed in this study occur within the shallow interiors of both Uranus and Neptune, pointing to other reasons for the differences in their luminosity [13]. The shallower diamond formation depth leads to greater potential heating as the diamond will subduct further. Our results place diamond formation above the proposed superionic ice layer [43–45]. Diamond-rich subduction plumes resulting from

demixing can thus occur in the electrically conductive ices, where they can contribute to the convective flow and dynamo activity which is believed to be responsible for the complex multipolar magnetic fields of the ice giants [45–49].

The lower pressure-temperature conditions also relax constraints on the size of astronomical body in which hydrocarbons would form diamonds. While 10 GPa is higher pressure than occurs in any moons in our solar system, many exoplanets have been discovered with sizes between Earth and Neptune and densities consistent with icy compositions [14]. These so called 'mini-Neptunes' make up one of the largest groups of exoplanets discovered and, being both plentiful and composed substantially of water, are of wide interest. The generation of diamonds within them could drive geodynamics, and have potential effects their atmospheric composition and planetary evolution [14, 50].

In conclusion, we have observed diamond formation on 30 µs timescales from polystyrene at 19 to 27 GPa above 2500 K in XFEL heated DAC experiments. This avoids potential problems with prior optical laser heated DAC studies and shows the discrepancy in diamond formation conditions determined in static and shock compression to be due to the drastically differing experimental timescales. This implies significant differences in chemical alteration, diamond formation, and equation of state for dynamic loading of CH bearing materials on different timescales, such as between nanosecond laser and microsecond impact compression experiments, and geophysical events on longer timescales. The conditions determined are consistent with diamond formation in both Uranus and Neptune at shallow depth, such that diamond precipitation may have a considerable evolutionary or present role in planetary dynamics. It also allows for diamond formation in much smaller icy bodies, which are observed to be a common class of exoplanet.

METHODS

Polystyrene film was compressed using a diamond anvil cell (DAC) equipped with Boehler-Almax geometry anvils with 400 µm culets and a rhenium gasket preindented to 60 µm thickness. A schematic of the loading is shown in Figure 2. Two layers of polystyrene were loaded sandwiching a perforated 5 µm gold foil coupler, with a small ruby sphere included for pressure determination [51]. In addition, a flake of amorphous boron was included as a laser coupler and can be seen as the powdery material in the micrograph

of the sample in Figure 2. This was not used, and is spatially separate from the gold so played no part in the experiment.

The polystyrene acts as the sample, pressure medium and insulation. In XFEL heated DAC samples it is necessary to provide a thermal barrier between the high Z coupler and diamonds to prevent anvil failure and maintain heat in the sample [29, 30]. The gold coupler was laser cut [52] with approximately 10 µm perforations spaced at 20 µm. These are sized such that the edges of the XFEL beam will be absorbed and heat the gold, while the center of the beam probes the heated sample. The hole spacing is adequate to minimize heating of adjacent holes. Gold was chosen as it has no known compounds with hydrogen or carbon and its diffraction peaks do not coincide with those of diamond, but it is high Z so effectively absorbs the X-rays.

Samples were prescreened at PETRA III beamline P02.2 using 0.4845 Å radiation collected on a Perkin Elmer XRD 1621 large area detector [53] . This confirmed the polystyrene to be non-crystalline with the only observable diffraction peaks arising from the gold coupler. The pressure obtained from the equation of state [34] of the gold coupler was 25(1) GPa. Integrated diffraction patterns from the prescreening are shown in Supplementary Figures 1 and 2.

The X-ray free electron laser pump-probe experiment was performed at the HED instrument of European XFEL [29] using 0.6965 Å (17.8 keV) radiation delivered in <50 fs pulses. Pulse trains consisted of up to 352 X-ray pulses delivered at 4.5 MHz for an inter-pulse spacing of 220 ns. The beam was focused using compound refractive lenses to a nominal 8 µm full width half maximum spot. The diffraction pattern from each pulse was individually collected on the large area AGIPD detector [54, 55] with pixel size 200 µm at a distance of 390 mm covering an angular range of 8.2° to 26.0° (corresponding to q = 1.29 to 4.06 Å^{-1}; d = 1.55 to 4.87 Å). By collecting individual diffraction patterns from each pulse we effectively probe the state obtained from the previous heating pulse and perform the heating for the next measurement in each pulse. This leads to an initial stepwise temperature increase which rapidly saturates [29, 30].

Figure 4 shows integrated X-ray diffraction patterns taken at the XFEL before, during and after heating. As well as the peaks from the gold coupler and the diamond formed there is a broad peak at around q = 3.02 Å^{-1} which is the {101} reflection from the rhenium gasket. This arises from low intensity fringes which extend significantly beyond the focused

section of the XFEL beam hitting the gasket and is observed in all XFEL shots. The {101} reflection is the strongest of rhenium [56], and no other peaks from the gasket are observable. It is not observed in the prescreening data from PETRA III (Supplementary Figures 1 and 2) as this beam passes though a pinhole. A pinhole was not used with the XFEL beam due to spatial fluctuations between the pulses. Additional data are presented in Supplementary Figures 3 and 4 and in Supplementary Table 1.

The total energy per pulse was controlled using absorbers. The full pulse energy was 306(23) µJ measured by the beam intensity monitoring diode which is calibrated using an absolutely-calibrated X-ray gas monitor [57], the pulse energies for a the rune presented in Figure 3 are shown in Supplementary Figure 5. Higher transmissions ($\geq$5%) cause measurable heating of the gold coupler and corresponding changes in the sample. Very low transmissions (0.5 to 1%) caused negligible heating and were used to probe the quenched sample after the high-temperature pump-probe experiment. A new coupler hole was used for each pump-probe experiment, such that each heating X-ray pulse train was incident on fresh material and any transformations can be ascribed to it alone. The starting pressure for a run was determined from positions of the gold peaks in the first pulse which probes the unheated material. This varied between runs due to pressure gradients across the DAC sample and the cell relaxing to lower pressure over the course of the experiment. The load on the cell was not adjusted during the experiment. In addition to the transmission, the energy absorbed, and hence degree of heating, depends on the geometry of the hole in the coupler and the beam pointing. For this reason higher transmission runs usually yielded higher temperatures, but not universally.

Raman spectra were taken of the sample after removal form the DAC using a 514 nm Ar-ion excitation laser in a micro-Raman system. Due to the localized heating the Raman spectrum of the heated region includes signal from unheated material which was further from the coupler. Raman spectra of the material in the DAC was not obtained as the anvils cracked when the XFEL beam intensity was increased to 50%.

Temperature was measured from the upstream side of the DAC using streaked optical pyrometry (SOP) [31, 33] with a time window of 97.4 µs, covering the duration of the heating. The field of view is 50 µm, though SOP is most sensitive to the hottest part of this area so effectively measures the temperature of the hot spot. Temperature and emissivity are both fitted as free parameters in a series of time steps across the streak image via a

Planck distribution between 575 and 800 nm (Supplementary Figures 6-8). In XFEL heated DACs temperature rises rapidly over the first few pulses before saturating [30]. The arrival of the first XFEL pulse coincides with the start of the initial rise in thermal emission, see Figure 3. The emissivity of both gold and the unheated polystyrene is very low and the intensity of the blackbody radiation increases over the first 10 µs along with other changes in the sample. The emissivity shown in Figure 3 is normalized to plateau near 1, which is likely close to the real emissivity due to the black state of the sample produced by heating. This darkening and change in emissivity is likely is due to initial reactions prior to diamond formation. The uncertainties in emissivity are assessed from a combination of fitting error and variations between two runs using the same beam transmission (25%) which are shown in Supplementary Figure 9. It should be noted that SOP is a surface probe and, as the polystyrene is darkened after heating, it is possible that some material close to the coupler reaches higher temperature but is obscured by opaque material further from the coupler. Extended Data Figure 1 shows a thermal cross-section of the sample based on FEA simulation which illustrates this.

The thermal equation of state of the gold coupler [34] offers a complementary temperature probe based on thermal expansion of the lattice. Temperature gradients in the coupler smear the diffraction peaks to lower q due to lattice expansion. The difficulty in fitting the peak, combined with possible thermal pressure [30, 58], results in a much larger uncertainty, typically $\sim$400 K, in the temperature measured by the gold coupler than by the SOP. This uncertainty arises from choice of equation of state, fitting of the diffraction peak, which has a skewed shape from thermal gradients, and possible thermal pressure. The upper bound on temperature is obtained by assuming 3 GPa of thermal pressure [30, 58] and fitting the low q edge of the gold peaks. The lower bounds assumes thermal pressure fully relaxes during the 220 ns between pulses. Positions assigned to the low q edge of this peak are shown in Supplementary Figure 10.

Figure 3 shows the temperature obtained from the gold equation of state to be systematically lower than that determined via SOP. This is expected as the sample is heated in very short bursts by the XFEL pulses with cooling between them, so the temperature has a saw-tooth profile [29, 30]. The SOP is most sensitive at highest temperature where emission is brightest, while the XFEL pulse probes the sample at the coolest point on each period. In addition to the temporal differences there are also spatial differences in the techniques. SOP

is a surface probe, while X-ray diffraction probes the bulk. Further data and fits from the SOP are presented in the Supplementary Materials Section IV. The temperatures quoted are those determined by SOP. The temperature measurable using diffraction from the gold coupler is limited by the melting point of gold, about 2200 to 2500 K for the pressures in this study [35, 36].

The thermal evolution of the sample was modeled using finite element analysis (FEA) simulation of the first 300 pulses. FEA simulations were performed in two-dimensional geometry with rotation symmetry around the XFEL beam and coupler hole, with thermal transport both parallel and perpendicular to the beam [30, 59]. Results are shown in Figure 3d, with further results presented in the Supplementary Materials section VI. The model parameters are presented in Supplementary Table 2. Sample heating is introduced mainly by the repeated direct heating of the coupler by the beam edges and gradual indirect heating of the sample cavity (Extended Data Figure 1 and Supplementary Figure 11). FEA temperatures agree well with experimental observations, reaching a stable temperature of 2500 K within $\sim 10\mu$s (~ 50 pulses) due to balance of cooling and heating rates [30]. The sample is observed to reach this temperature at shorter times than the model predicts, which we attribute to initial misalignment between the sample hole and XFEL beam such that the first pulse is not perfectly centered on the hole and so deposits more energy into the coupler, followed by rapid migration of hot gold [59] away from the beam. The stronger gold diffraction from the initial pulse compared to subsequent pulses supports this interpretation (Supplementary Figure 4), suggesting the hole rapidly reformed around the beam on initial heating leading to improved model agreement on longer timescale.

Correspondence and requests for materials should be addressed to Mungo Frost.

Data availability: The datasets used during the current study are available from the corresponding author on reasonable request.

Acknowledgements: The authors would like to thank Nicholas Hartley for fruitful discussions. This work was supported by U.S. Department of Energy (DOE) Office of Fusion Energy Sciences funding No. FWP100182. AFG and EE are grateful for support of Carnegie Science and NSF EAR-2049127. We acknowledge European XFEL in Schenefeld, Germany, for provision of X-ray free-electron laser beamtime at Scientific Instrument HED and would like to thank the staff for their assistance. We acknowledge DESY (Hamburg, Germany), a member of the Helmholtz Association HGF, for the provision of experimental

facilities. Parts of this research were carried out at PETRA III beamline P02.2. Beamtime was allocated from In House beamtime from the beamline. Lawrence Livermore National Laboratory is operated by Lawrence Livermore National Security, LLC, for the U.S. Department of Energy (DOE), National Nuclear Security Administration under Contract DE-AC52-07NA27344. SN and LA acknowledge financial support from Sorbonne University under grant Emergence HP-XFEL. YL is grateful for support from the Leader Researcher program (NRF-2018R1A3B1052042) of the Korean Ministry of Science and ICT (MSIT). The authors are indebted to the HIBEF user consortium for the provision of instrumentation and staff that enabled this experiment. GM has been supported by a grant from Labex OSUG@2020 (Investissements d'avenir – ANR10 LABX56) and PNP-INSU program. MB acknowledges the support of Deutsche Forschungsgemeinschaft (DFG Emmy-Noether project BY112/2-1).

Author Contributions: All authors were involved in experimental planning. MF, EB, MB, RJH, CS, HPL, ZK and AFG coordinated the experiment. MF prepared the samples. HPL, JDH, LMA, SK and BM performed the prescreening at P02.2 at PETRA III. MF, CS, CB, HPL, ZK, SN, JDH, CP, EE, RSM, SC, OB, MD and AFG conducted the experiment. TL, SS, CS and JSD operated the AGIPD detector. RR, SHG and AFG advised. MF, RSM, OBB, RJH, ZK, CP, EE and AFG analyzed the data. MF and RSM wrote the manuscript.

Competing Interests: The authors declare no competing interests.

[1] Bethkenhagen, M. *et al.* Planetary ices and the linear mixing approximation. *Astrophys. J.* **848**, 67 (2017).

[2] Scheibe, L., Nettelmann, N. & Redmer, R. Thermal evolution of uranus and neptune-i. adiabatic models. *Astron. Astrophys.* **632**, A70 (2019).

[3] Qasim, D. *et al.* An experimental study of the surface formation of methane in interstellar molecular clouds. *Nat. Astron.* **4**, 781–785 (2020).

[4] Benedetti, L. R. *et al.* Dissociation of ch4 at high pressures and temperatures: diamond formation in giant planet interiors? *Science* **286**, 100–102 (1999).

[5] Hirai, H., Konagai, K., Kawamura, T., Yamamoto, Y. & Yagi, T. Polymerization and diamond formation from melting methane and their implications in ice layer of giant planets. *Phys.*

Earth Planet. Inter. **174**, 242–246 (2009).

[6] Kraus, D. *et al.* Formation of diamonds in laser-compressed hydrocarbons at planetary interior conditions. *Nat. Astron.* **1**, 606–611 (2017).

[7] Cheng, B., Hamel, S. & Bethkenhagen, M. Thermodynamics of diamond formation from hydrocarbon mixtures in planets. *Nat. Commun.* **14**, 1104 (2023).

[8] Lobanov, S. S. *et al.* Carbon precipitation from heavy hydrocarbon fluid in deep planetary interiors. *Nat. Commun.* **4**, 1–8 (2013).

[9] Kolesnikov, A., Kutcherov, V. G. & Goncharov, A. F. Methane-derived hydrocarbons produced under upper-mantle conditions. *Nat. Geosci.* **2**, 566–570 (2009).

[10] Spanu, L., Donadio, D., Hohl, D., Schwegler, E. & Galli, G. Stability of hydrocarbons at deep earth pressures and temperatures. *Proc. Natl. Acad. Sci. U.S.A.* **108**, 6843–6846 (2011).

[11] Naumova, A. S., Lepeshkin, S. V. & Oganov, A. R. Hydrocarbons under pressure: Phase diagrams and surprising new compounds in the c–h system. *J. Phys. Chem. C* **123**, 20497–20501 (2019).

[12] Ross, M. The ice layer in uranus and neptune—diamonds in the sky? *Nature* **292**, 435–436 (1981).

[13] Podolak, M. & Helled, R. What do we really know about uranus and neptune? *Astrophys. J. Lett.* **759**, L32 (2012).

[14] Piette, A. A. & Madhusudhan, N. On the temperature profiles and emission spectra of mini-neptune atmospheres. *Astrophys. J.* **904**, 154 (2020).

[15] Jiang, S. *et al.* A spectroscopic study of the insulator–metal transition in liquid hydrogen and deuterium. *Adv. Sci.* **7**, 1901668 (2020).

[16] He, Z. *et al.* Diamond formation kinetics in shock-compressed c-h-o samples recorded by small-angle x-ray scattering and x-ray diffraction. *Sci. Adv.* **8**, eabo0617 (2022).

[17] Wang, X., Scandolo, S. & Car, R. Carbon phase diagram from ab initio molecular dynamics. *Phys. Rev. Lett.* **95**, 185701 (2005).

[18] Nettelmann, N. *et al.* Theory of figures to the seventh order and the interiors of jupiter and saturn. *Planet. Sci. J.* **2**, 241 (2021).

[19] Scheler, T. *et al.* Synthesis and properties of platinum hydride. *Phys. Rev. B* **83**, 214106 (2011).

[20] Frost, M., McBride, E. E., Smith, D., Smith, J. S. & Glenzer, S. H. Pressure driven alkane

dehydrogenation by palladium metal. *Adv. Mater. Interfaces* **10**, 2202081 (2023).

[21] Zerr, A., Serghiou, G., Boehler, R. & Ross, M. Decomposition of alkanes at high pressures and temperatures. *High Press. Res.* **26**, 23–32 (2006).

[22] Watkins, E. *et al.* Diamond and methane formation from the chemical decomposition of polyethylene at high pressures and temperatures. *Sci. Rep.* **12**, 1–8 (2022).

[23] Hartley, N. *et al.* Evidence for crystalline structure in dynamically-compressed polyethylene up to 200 gpa. *Sci. Rep.* **9**, 1–7 (2019).

[24] Seiboth, F. *et al.* Simultaneous 8.2 kev phase-contrast imaging and 24.6 kev x-ray diffraction from shock-compressed matter at the lcls. *Appl. Phys. Lett.* **112**, 221907 (2018).

[25] Zylstra, A. *et al.* Burning plasma achieved in inertial fusion. *Nature* **601**, 542–548 (2022).

[26] Kraus, D. *et al.* High-pressure chemistry of hydrocarbons relevant to planetary interiors and inertial confinement fusion. *Phys. Plasmas* **25**, 056313 (2018).

[27] Nestola, F. *et al.* Impact shock origin of diamonds in ureilite meteorites. *Proc. Natl. Acad. Sci. U.S.A.* **117**, 25310–25318 (2020).

[28] Zastrau, U. *et al.* The high energy density scientific instrument at the european xfel. *J. of Synchrotron Radiat.* **28**, 1393–1416 (2021).

[29] Liermann, H.-P. *et al.* Novel experimental setup for megahertz x-ray diffraction in a diamond anvil cell at the high energy density (hed) instrument of the european x-ray free-electron laser (euxfel). *J. of Synchrotron Radiat.* **28**, 688–706 (2021).

[30] Meza-Galvez, J. *et al.* Thermomechanical response of thickly tamped targets and diamond anvil cells under pulsed hard x-ray irradiation. *J. of Appl. Phys.* **127**, 195902 (2020).

[31] Ball, O. B. *et al.* Dynamic optical spectroscopy and pyrometry of static targets under optical and x-ray laser heating at the European XFEL. *J. of Appl. Phys.* **134**, 055901 (2023).

[32] McWilliams, R. S., Dalton, D. A., Konôpková, Z., Mahmood, M. F. & Goncharov, A. F. Opacity and conductivity measurements in noble gases at conditions of planetary and stellar interiors. *Proc. Natl. Acad. Sci. U.S.A.* **112**, 7925–7930 (2015).

[33] McWilliams, R. S., Dalton, D. A., Mahmood, M. F. & Goncharov, A. F. Optical properties of fluid hydrogen at the transition to a conducting state. *Phys. Rev. Lett.* **116**, 255501 (2016).

[34] Anderson, O. L., Isaak, D. G. & Yamamoto, S. Anharmonicity and the equation of state for gold. *J. of Appl. Phys.* **65**, 1534–1543 (1989).

[35] Zha, C.-S. & Bassett, W. A. Internal resistive heating in diamond anvil cell for in situ x-ray

diffraction and raman scattering. *Rev. Sci. Instrum.* **74**, 1255–1262 (2003).

[36] Weck, G. *et al.* Determination of the melting curve of gold up to 110 gpa. *Phys. Rev. B* **101**, 014106 (2020).

[37] Hubbard, W. Neptune's deep chemistry. *Science* **275**, 1279–1280 (1997).

[38] Knudson, M. D. *et al.* Direct observation of an abrupt insulator-to-metal transition in dense liquid deuterium. *Science* **348**, 1455–1460 (2015).

[39] Zaghoo, M. & Silvera, I. F. Conductivity and dissociation in liquid metallic hydrogen and implications for planetary interiors. *Proc. Natl. Acad. Sci. U.S.A.* **114**, 11873–11877 (2017).

[40] Celliers, P. M. *et al.* Insulator-metal transition in dense fluid deuterium. *Science* **361**, 677–682 (2018).

[41] Kraus, D. *et al.* Indirect evidence for elemental hydrogen in laser-compressed hydrocarbons. *Phys. Rev. Res.* **5**, L022023 (2023).

[42] Correa, A. A., Bonev, S. A. & Galli, G. Carbon under extreme conditions: Phase boundaries and electronic properties from first-principles theory. *Proc. Natl. Acad. Sci. U.S.A.* **103**, 1204–1208 (2006).

[43] Millot, M. *et al.* Nanosecond x-ray diffraction of shock-compressed superionic water ice. *Nature* **569**, 251–255 (2019).

[44] Weck, G. *et al.* Evidence and stability field of fcc superionic water ice using static compression. *Phys. Rev. Lett.* **128**, 165701 (2022).

[45] Prakapenka, V. B., Holtgrewe, N., Lobanov, S. S. & Goncharov, A. F. Structure and properties of two superionic ice phases. *Nat. Phys.* **17**, 1233–1238 (2021).

[46] Stanley, S. & Bloxham, J. Convective-region geometry as the cause of uranus' and neptune's unusual magnetic fields. *Nature* **428**, 151–153 (2004).

[47] Cavazzoni, C. *et al.* Superionic and metallic states of water and ammonia at giant planet conditions. *Science* **283**, 44–46 (1999).

[48] Redmer, R., Mattsson, T. R., Nettelmann, N. & French, M. The phase diagram of water and the magnetic fields of uranus and neptune. *Icarus* **211**, 798–803 (2011).

[49] Soderlund, K. & Stanley, S. The underexplored frontier of ice giant dynamos. *Philos. Trans. Royal Soc. A* **378**, 20190479 (2020).

[50] Hörst, S. M. *et al.* Haze production rates in super-earth and mini-neptune atmosphere experiments. *Nat. Astron.* **2**, 303–306 (2018).

[51] Dewaele, A., Torrent, M., Loubeyre, P. & Mezouar, M. Compression curves of transition metals in the mbar range: Experiments and projector augmented-wave calculations. *Phys. Rev. B* **78**, 104102 (2008).

[52] Frost, M., Curry, C. & Glenzer, S. Laser cutting apparatus for high energy density and diamond anvil cell science. *J. Instrum.* **15**, P05004 (2020).

[53] Liermann, H.-P. *et al.* The extreme conditions beamline p02. 2 and the extreme conditions science infrastructure at petra iii. *J. of Synchrotron Radiat.* **22**, 908–924 (2015).

[54] Allahgholi, A. *et al.* Agipd, a high dynamic range fast detector for the european xfel. *J. Instrum.* **10**, C01023 (2015).

[55] Allahgholi, A. *et al.* The adaptive gain integrating pixel detector at the european xfel. *J. of Synchrotron Radiat.* **26**, 74–82 (2019).

[56] Scheler, T., Degtyareva, O. & Gregoryanz, E. On the effects of high temperature and high pressure on the hydrogen solubility in rhenium. *J. Chem. Phys.* **135**, 214501 (2011).

[57] Maltezopoulos, T. *et al.* Operation of x-ray gas monitors at the european xfel. *J. of Synchrotron Radiat.* **26**, 1045–1051 (2019).

[58] Dewaele, A., Fiquet, G. & Gillet, P. Temperature and pressure distribution in the laser-heated diamond–anvil cell. *Rev. Sci. Instrum.* **69**, 2421–2426 (1998).

[59] Husband, R. J. *et al.* X-ray free electron laser heating of water and gold at high static pressure. *Commun. Mater.* **2**, 1–9 (2021).

EXTENDED DATA FIGURES

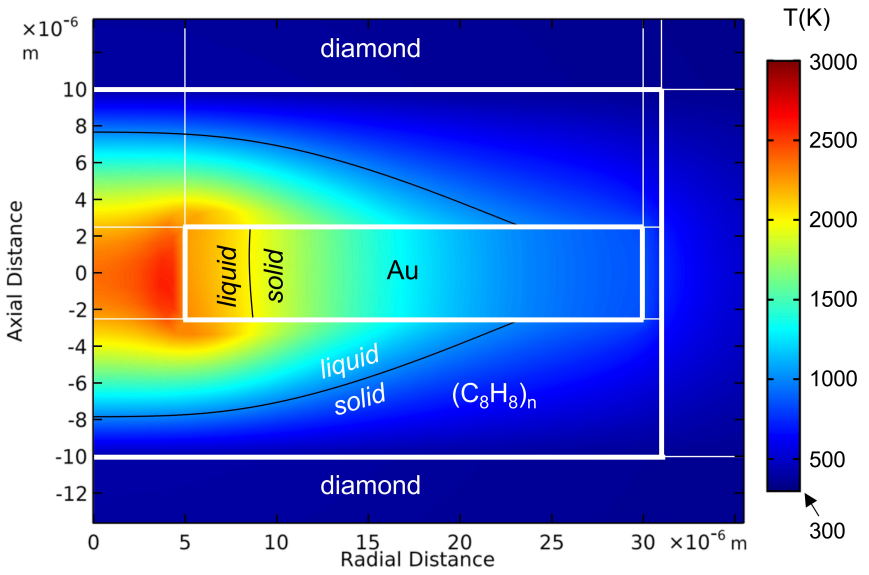

EXTENDED DATA FIG. 1. FEA model (cylindrical section) of sample temperature at the time of XFEL probing at ∼30 μs in Figure 3d. Bold white lines indicate boundaries between DAC components; light white lines indicate additional boundaries required by the analysis; XFEL radiation is from below [30]. Black lines indicate solid-liquid boundaries, with the melting point of Au taken to be 2350 K [35, 36] and the melting point of polystyrene taken to be 1000 K (representing a likely minimum bound, considering an ambient melting point of 510 K and steep rise with pressure). The model shows high temperatures are localized near the coupler hole, with cold material surrounding the hotspot, including several microns of cold and solid polystyrene separating the sample from the diamond anvils and significantly more separating the hot sample from the gasket.

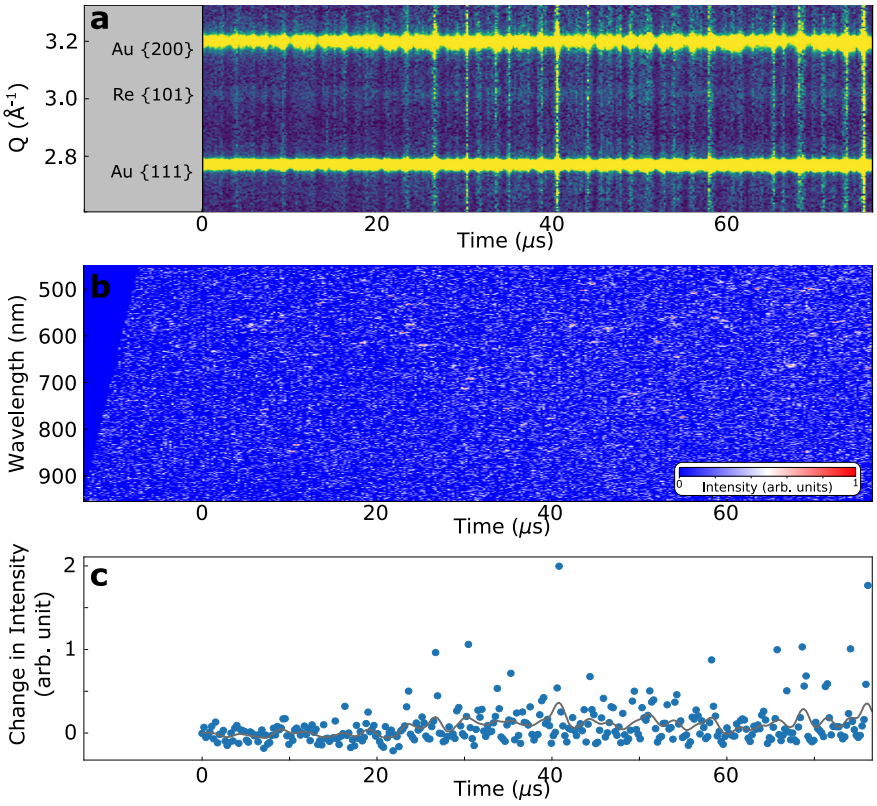

EXTENDED DATA FIG. 2. Time resolved data from a run with 1% beam power. No thermal emission or diamond is observed. **a:** XRD in region of interest, vertical stripes are artifacts from diode normalization. **b:** SOP spectrogram showing no emission. **c:** Time evolution of intensity at q where diamond is expected shows no diamond formation, the line is smoothed with 15 pulse wide Hamming window. Time 0 is estimated first arrival of X-rays based on other runs.

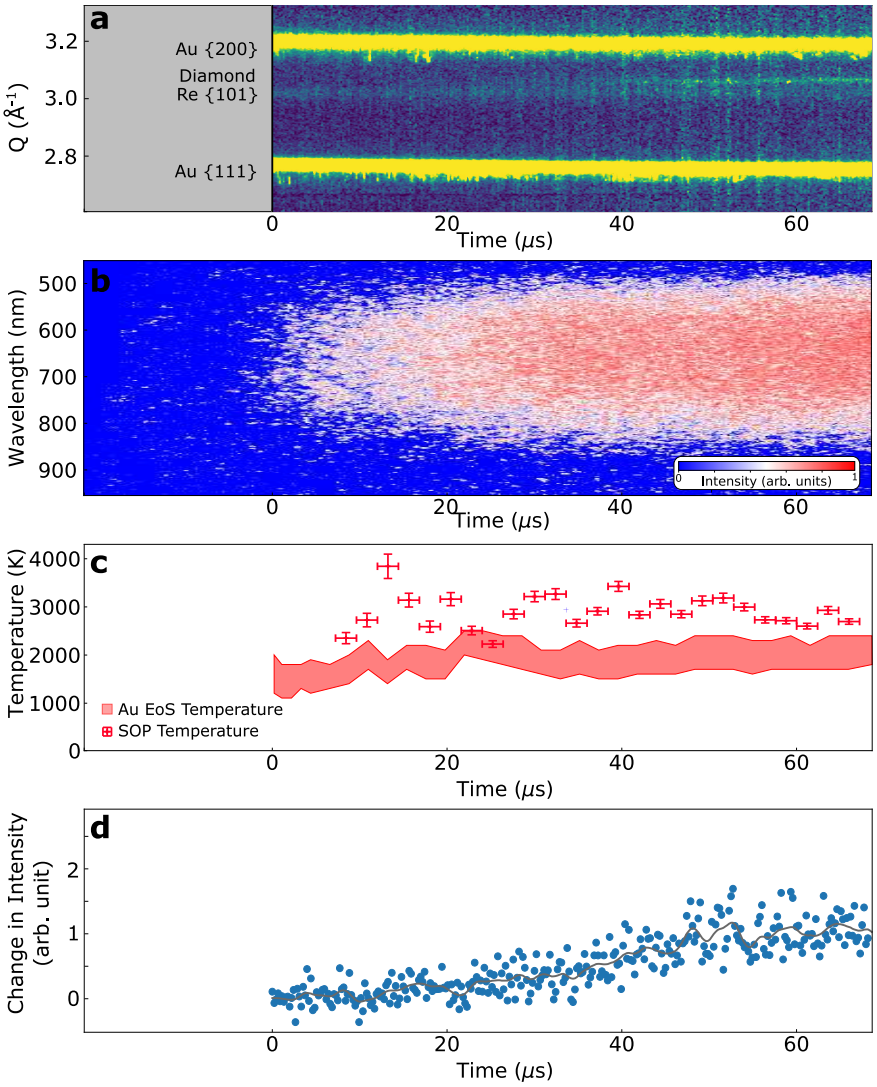

EXTENDED DATA FIG. 3. Time resolved data from a run with 5% beam power. Thermal emission and diamond formation are observed. **a:** XRD in region of interest normalized to beam intensity monitoring diode. The diamond {111} reflection is visible after 40 µs. **b:** SOP spectrogram. **c:** Temperature from SOP fitting and equation of state of gold [34]. **d:** Time evolution of diamond peak intensity, line is smoothed with 15 pulse wide Hamming window. Time 0 corresponds to first X-ray pulse based on rising edge of thermal emission. Temporal error bars represent the time bin of the SOP, temperature error bars represent one-half standard deviation confidence and are derived from the fitting uncertainty of a Planck function to the spectrographic data and statistical analysis of these data [31].

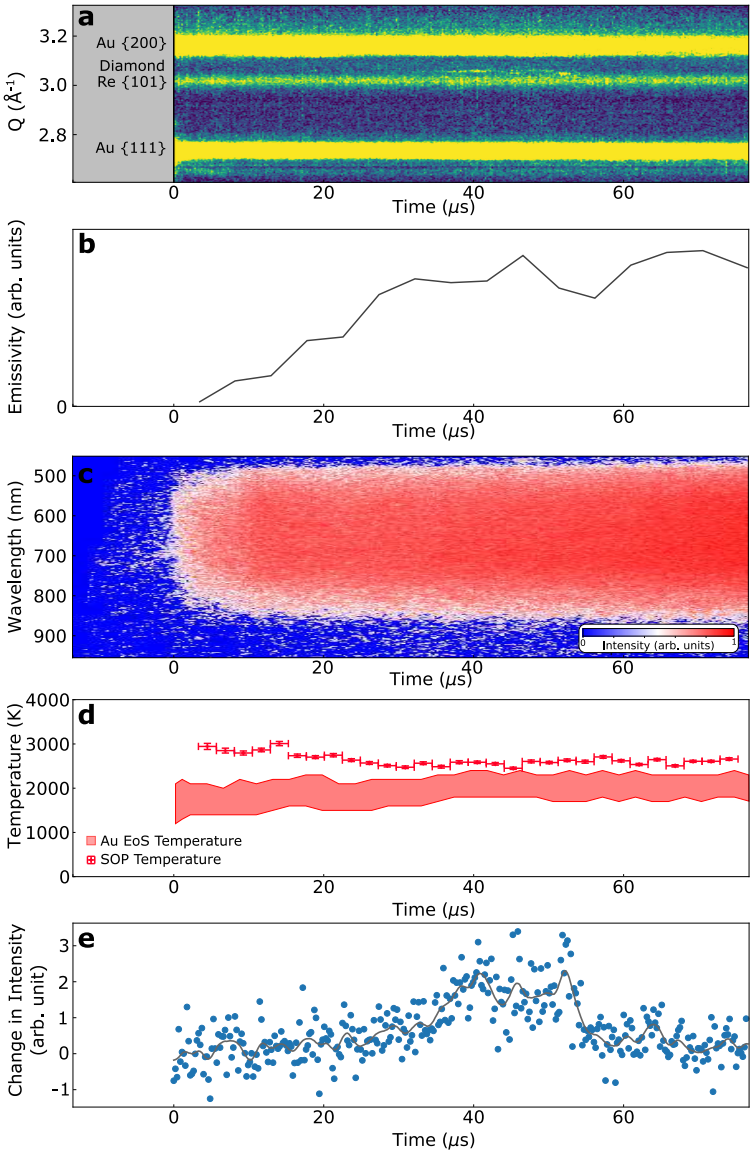

EXTENDED DATA FIG. 4. Time resolved data from a run with 25% beam power. This is a different run than is presented in Figure 3, but shows similar temperatures and diamond formation. **a:** XRD in region of interest normalized to beam intensity monitoring diode. The diamond {111} reflection is visible after 35 µs. **b:** Emissivity as a function of time. **c:** SOP spectrogram. **d:** Temperature from SOP fitting and equation of state of gold [34]. **d:** Time evolution of diamond peak intensity, line is smoothed with 15 pulse wide Hamming window. Time 0 corresponds to first X-ray pulse based on rising edge of thermal emission. Temporal error bars represent the time bin of the SOP, temperature error bars represent one-half standard deviation confidence and are derived from the fitting uncertainty of a Planck function to the spectrographic data and statistical analysis of these data [31].

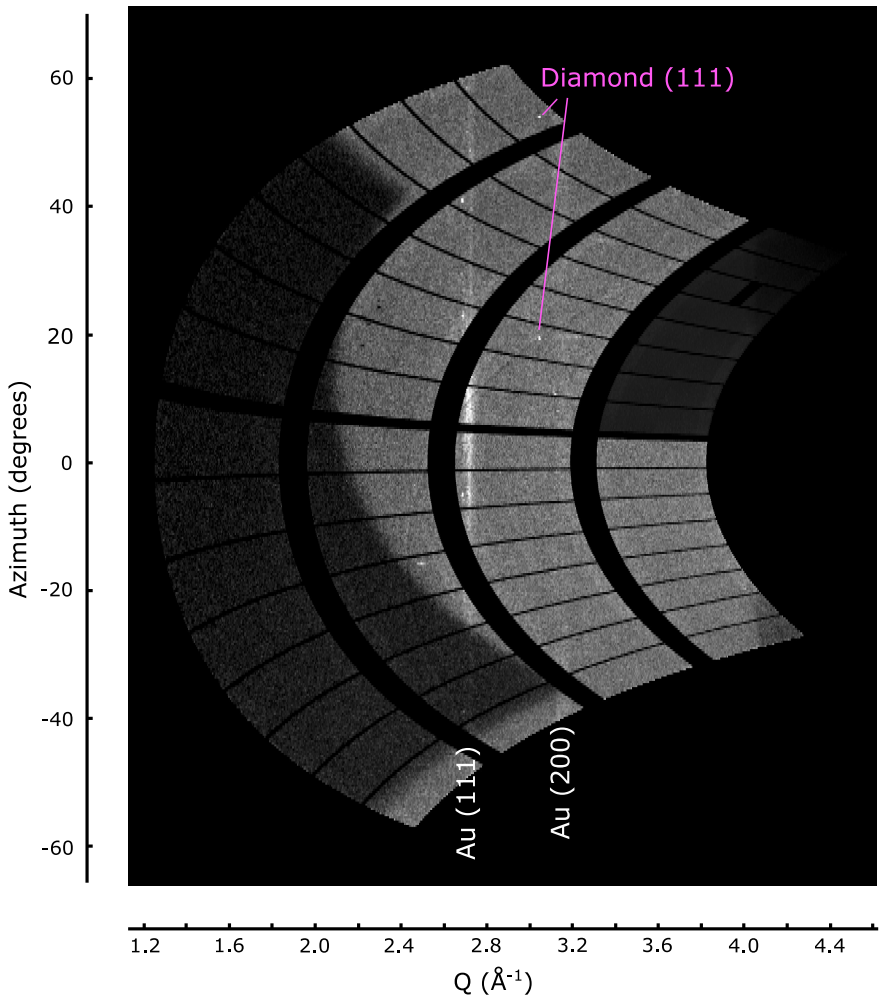

EXTENDED DATA FIG. 5. Raw diffraction pattern from a single XFEL pulse taken 40.2 µs into a run starting at 19 GPa. The SOP temperature is 2540(30) K. The integrated pattern is shown in Figure 4b. $\lambda = 0.6965$ Å. Lighter shades correspond to higher signal, brightness and contrast are optimized for visibility. The pattern is azimuthally unwrapped such that vertical lines are at constant q (also known as 'caked'). The shadow at low q is from the mirror used to observe the sample, the dark panel (top right) was faulty and masked when integrating the diffraction patterns.